LINEAR ARRAY SAR IMAGING VIA COMPRESSED SENSING

S.-J. Wei [*], X.-L. Zhang, and J. Shi

School of Electronic Engineering, University of Electronic Science and Technology of China, Chengdu 611731, China

Abstract—In recent years, various attempts have been undertaken to obtain three-dimensional (3-D) reflectivity of observed scene from synthetic aperture radar (SAR) technique. Linear array SAR (LASAR) has been demonstrated as a promising technique to achieve 3-D imaging of earth surface. The common methods used for LASAR imaging are usually based on matched filter (MF) which obeys the traditional Nyquist sampling theory. However, due to limitation in the length of linear array and the "Rayleigh" resolution, the standard MF-based methods suffer from low resolution and high sidelobes. Hence, high resolution imaging algorithms are desired. In LASAR images, dominating scatterers are always sparse compared with the total 3-D illuminated space cells. Combined with this prior knowledge of sparsity property, this paper presents a novel algorithm for LASAR imaging via compressed sensing (CS). The theory of CS indicates that sparse signal can be exactly reconstructed in high Signal-Noise-Ratio (SNR) level by solving a convex optimization problem with a very small number of samples. To overcome strong noise and clutter interference in LASAR raw echo, the new method firstly achieves range focussing by a pulse compression technique, which can greatly improve SNR level of signal in both azimuth and cross-track directions. Then, the resolution enhancement images of sparse targets are reconstructed by L1 norm regularization. High resolution properties and point localization accuracies are tested and verified by simulation and real experimental data. The results show that the CS method outperforms the conventional MF-based methods, even if very small random selected samples are used.

1. INTRODUCTION

Three-dimensional (3-D) synthetic aperture radar (SAR) imaging has received a growing interest recently. Compared with 2-D images received by traditional SAR technology [1–4], 3-D SAR images of illuminated scene can give much more details to understand and identify target characteristics, which are significant for many important civilian and military applications (such as 3-D digital maps, stereo city, target detection and identification, and flight navigation). Hence, 3-D SAR is an emerging research field and will play an important role in the next SAR products.

Up to now, some different 3-D SAR imaging techniques have been proposed. The most popular SAR 3-D imaging technique is interferometric SAR (InSAR) [5–7]. But InSAR cannot extract the heights of different scatterers in the same range-azimuth cell. In the past decade, Tomographic SAR (TomoSAR) technique has been presented, which extends the synthetic aperture principle into the elevation by slightly different multi-pass track [8, 9]. TomoSAR allows to extract different height scatterers in each given range-azimuth cell and provides the true 3-D images of illuminated scene. However, TomoSAR suffers from some obvious defects, e.g., shadow, layover, geometrical deformation in image due to working in the side-looking mode [10], and high cost due to a large number of repeat-passes. These defects result in that TomoSAR cannot be widely applied in practice. To overcome above-mentioned disadvantages of TomoSAR, a new linear array SAR (LASAR) down-looking 3-D imaging technique has been developed in recent years [11, 12]. LASAR obtains range resolution by pulse compression of chirp echo signal and receives azimuth and cross-track (CT) dimensional resolution from a 2-D virtual aperture which is formed by a linear array antenna (LAA) movement perpendicular to flight direction. Unlike TomoSAR restricted by the side-looking mode, LASAR can work in a flexible mode, including side-looking, forward-looking and down-looking. Nowadays, some standard algorithms have been developed for LASAR 3-D imaging, such as 3-D Range-Doppler algorithm [13], Chirp Scaling algorithm [14], and 3-D Back-Projection algorithm [15]. But these algorithms are mostly based on data independent matched filter (MF) theorem which requires a large number of uniform samples to obey the Nyquist rate. In addition, the focussing of LASAR data based on MF-based methods is usually analogous to SINC function and limited by the "Rayleigh" resolution, and generates a value of $-13.4\,\text{dB}$ sidelobe fuzzy [16, 17]. Hence, though simple to implement and fast to computation, MF-based methods suffer from low resolution and high

sidelobe interference in the images. Moreover, the resolution of MF-based methods in azimuth-CT directions depends on the size of 2-D synthetic aperture plane. Therefore, to achieve high resolution by MF-based methods in azimuth-CT directions, a large virtual 2-D aperture is required. Specially, the required length of LAA must be always tens or even hundreds of meters. In practice, due to the platform size and load restraint, the length of this fixed LAA is limited to several meters. Then the 2-D virtual aperture is not large enough for achieving a satisfactory resolution value in azimuth-CT plane, and CT resolution is often at least an order of magnitude lower than resolution in range direction. Hence, how to improve imaging resolution with the limited length of LAA is the main problem of LASAR 3-D imaging at present.

In recent years, an emerging theory of compressed sensing (CS) has caused widespread concern, which brings about a revolutionary breakthrough to sparse signal reconstruction [18, 19]. In CS, the compressible signal can be exactly recovered by incoherent linear projection using just a small number of random measurements. Now CS has been discussed and studied widely in different areas, including medical imaging, communications, image reconstruction, radar imaging, remote sensing, analog to information conversion. Some applications of CS in SAR imaging are also concerned about recently [20–24]. Most of these papers used CS to reconstruct high resolution image of sparse targets, such as ships, cars and aerial targets. In [25], we also analyzed high resolution properties of CS in SAR 2-D imaging, but the results demonstrate that CS method is sensitive to noise, and the exact reconstruction requires high SNR level (SNR $\geq 10\,\mathrm{dB}$) of raw echo. Nevertheless, the echo signals of SAR are always interfered by strong noise in actual circumstances. Hence, the high SNR is difficult to achieve for SAR raw echo. Furthermore, the 3-D illuminated scene has sparse property because it contains only a very small domain scatterers compared with the total space cells. But it is no longer sparse when projected onto the 2-D range-azimuth plane in traditional SAR. Then CS method fails in these "non-sparse" scenes imaging (such as mountains and urban areas) which are the main products of traditional SAR. Therefore, CS is more suitable for 3-D SAR than traditional SAR. An inversion approach to reconstruct elevation sparse scatterers based on CS has been presented for TomoSAR 3-D imaging in [26]. Its super-resolution properties in tomography elevation are demonstrated by TerraSAR-X data. In [27], a similar approach for TomoSAR elevation reconstruction using CS was presented, and its performance was validated compared with the truncated singular value decomposition technique. However, these CS-based methods for TomoSAR imaging mentioned above only achieved

super-resolution for 1-D (elevation direction) targets reconstruction.

To overcome the disadvantages of MF-based methods and improve the imaging quality of LASAR, inspired by CS theory and combined with the sparse feature of 3-D scene, (i.e., only a few number of scatterers with the same height are present in the azimuth-CT plane), this paper presents a novel approach for LASAR 3-D imaging based on CS. In our case, sparseness requires a small number of scatterers in the same range cell. Instead of conventional sampling at Nyquist rate, only a small number of random selected samples are used for measurements.

The organization of the paper is as follows. Section 2 contains a brief description to LASAR data acquisition model and traditional MF-based imaging methods. Section 3 gives an introduction of CS basic theory and presents the 3-D imaging algorithm of LASAR via CS. Numerical simulated and real experimental results are presented in Section 4 along with a performance analysis. Finally, a summary is given in Section 5.

2. LASAR IMAGING MODEL

In this section, we mainly describe the principle of LASAR imaging, with special emphasis on the geometry and signal model. Suppose that LASAR works in down-looking mode. The simple geometrical model of LASAR is illustrated in Figure 1. The platform is moving along axis y corresponding to azimuth direction, at altitude H with constant velocity v. Axis x is CT direction which is parallel to LAA,
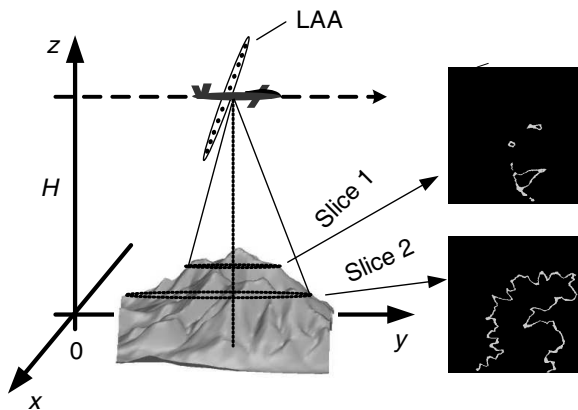
Figure 1. The geometric model of LASAR down-looking imaging.

and the height axis z denotes range direction. Hence, the image space coordinate of LASAR corresponds to Cartesian coordinate. The length of LAA is L_c with N_c elements. The interval of adjacent elements is d_i, with $i = 1, \ldots, N_c - 1$.

A reference point scatterer with radar cross section (RCS) $\sigma(\mathbf{P}_w)$ is supposed at position $\mathbf{P}_w = [x_s, y_s, z_s]^T$. At slow time n, the distance between scatter $\mathbf{P}_w$ and the ith LAA element is $R(n, i; \mathbf{P}_w) = \|\mathbf{P}_r(n, i) - \mathbf{P}_w\|_2$, and $\mathbf{P}_r(n, i) = [x_p, y_p, H]$ is position of the ith LAA element with $x_p = \sum\limits_{k=1}^{i} d_k$ and $y_p = vn$. Suppose that radar transmits a linear frequency modulated (LFM) signal [28, 29]. The received echo of the ith LAA element for the point scattering $\mathbf{P}_w$ can be expressed as

$$s_m(t, n, i; \mathbf{P}_w) = \alpha(\mathbf{P}_w) \exp(-j2\pi f_c \tau) \exp\left[j\pi f_{dr}(t - \tau)^2\right],$$
$$|t| \in T/2 \quad (1)$$

where f_c denotes carrier frequency; f_{dr} is LFM chirp rate; T is pulse repetition time; $\tau = 2R(n, i; \mathbf{P}_w)/C$ denotes the echo delay; C is the speed of light in air. The first exponent term contains the target's information in azimuth-CT plane [30, 31]. The second exponent term expresses the target's range information [32]. For a 3-D measured scene Ω, the received signal can be written as

$$S_c(t, n, i) = \int\limits_{\mathbf{P}_w \in \Omega} \alpha(\mathbf{P}_w) \exp(-j2\pi f_c \tau) \exp\left[j\pi f_{dr}(t - \tau)^2\right] d\mathbf{P}_w \quad (2)$$

If we separate the 3-D scene reflectivity into grid points of N' and express the measured samples with vector $\mathbf{S}_c$, we can parameterize (2) in terms of reflectivity vector $\mathbf{f} \in \mathbb{R}^{N'}$ and delay-Doppler function $\mathbf{A} \in \mathbb{C}^{N \times N'}$ as follow.

$$\mathbf{S}_c = \mathbf{A}\mathbf{f} \quad (3)$$

where $\mathbf{f} = [\alpha_1, \alpha_2, \ldots, \alpha_{N'}]^T$, $\mathbf{A} = \{\exp(-j2\pi f_c \tau_j) \exp[j\pi f_{dr}(t_i - \tau_j)^2]\}$, $1 \leq i \leq N$ and $1 \leq j \leq N'$.

The conventional MF-based methods for LASAR 3-D imaging are mainly achieved by signal autocorrelation to obtain the maximum SNR of output image [33–36]. The simple expression of output image for MF-based methods can be written as

$$\hat{\mathbf{f}} = \mathbf{A}^H \mathbf{A}\mathbf{f} \quad (4)$$

Because $\mathbf{A}^H \mathbf{A} \neq \mathbf{I}$ is not a unit matrix, the autocorrelation between the columns of matrix $\mathbf{A}$ could cause ambiguity for reflectivity $\mathbf{f}$

reconstruction. The detail focused signal of LASAR can be expressed as follow.

$$S_o(r, x, y) \approx \sum_{s=1}^{N} \sigma(\mathbf{P}_w) \exp\left(-j\frac{4\pi R_0}{\lambda}\right) \cdot \mathrm{sinc}\left(\frac{r - r_s}{\rho_r}\right)$$
$$\cdot \mathrm{sinc}\left(\frac{x - x_s}{\rho_c}\right) \cdot \mathrm{sinc}\left(\frac{y - y_s}{\rho_a}\right) \tag{5}$$

where the function $\mathrm{sinc}(x) = \sin(\pi x)/(\pi x)$. Then the resolution of range, azimuth and CT directions can be expressed respectively as bellow.

$$\rho_r = \frac{C}{2B_r}, \quad \rho_a = \frac{\lambda H}{2L_a}, \quad \rho_c = \frac{\lambda H}{2L_c} \tag{6}$$

where, B_r denotes the bandwidth of LFM signal; $L_a \approx \lambda H/D$ is the length of azimuth synthetic aperture; D denotes the real aperture of antenna; λ denotes radar wavelength.

From resolution formulas (5) and (6) of LASAR, the focused signals in azimuth and CT direction are similar, and both are SINC function, which suffer from high sidelobes interference. The CT resolution is determined by the length of LAA, and azimuth resolution depends on the length of synthetic aperture. In order to observe large area, LASAR platform must work at a high altitude. In this case, a large 2-D synthetic aperture on azimuth-CT plane is required to obtain high resolution. Then the length of LAA to form the 2-D synthetic aperture must be long enough. However, the length of LAA is limited by the platform in practice. So the 2-D resolution of azimuth-CT directions is often lower than that in the range. To overcome these disadvantages of conventional MF-based methods, a new imaging method of LASAR based on the theory of CS is introduced in the next section.

3. LASAR IMAGING VIA CS

CS is a new theory which enables the reconstruction of sparse signals to only a small number of linear measurements compared with traditional Nyquist rate. The theory of CS states that a K-sparse signal $\mathbf{a} = \Psi \mathbf{x}$ of length N in basis Ψ can be exactly recovered with high probability from $O(K \log(N/K))$ measurements by solving a convex optimization problem via l_1 norm [18]. The reconstruction step of CS can be simply formulated as follow.

$$\min \|\mathbf{x}\|_1 \quad \text{s.t} \quad \|\mathbf{y} - \Theta \mathbf{x}\|_2 < \varepsilon \tag{7}$$

where, $\mathbf{y} = \Phi \mathbf{a}$ is measurement vector with length M; $\Theta = \Phi \Psi \in \mathbb{R}^{M \times N}$ denotes the measurement matrix with $M \ll N$; ε bounds

the amount of noise in data. There are some sparse approximation algorithms to recover the sparse signal $\mathbf{x}$ from measurements $\mathbf{y}$ in (7) recently, including basis pursuit (BP) [37], orthogonal match-pursuit (OMP) [38], and regularized orthogonal matching pursuit (ROMP) [39].

However, to guarantee the stable solution for CS reconstruction, the following conditions must be hold [18]. First, the signal $\mathbf{a}$ must be sparse expression in the basis Ψ. Second, the sensing matrix Φ and the basis Ψ must be mutually incoherent. Third, the measurement matrix Θ must follow the restricted isometry property (RIP) requiring that $(1 - \delta_K)\|\eta\|_2^2 \leq \|\Theta\eta\|_2^2 \leq (1 + \delta_K)\|\eta\|_2^2$, where η is any vector having K nonzero coefficients, and $\delta_K \in (0, 1)$. The smaller the value δ_K is, the better the sparse signal can be reconstructed. The RIP is closely related to an incoherency property. When the measurement matrix is constructed by Gaussian random matrices or random partial Fourier basis, it performs well for RIP [40].

The first prerequisite for CS reconstruction is that the signal must be sparse or compressible in some representation. Mostly this premise of CS cannot be met in traditional SAR 2-D imaging, because its target space is non-sparse after the 3-D illuminated scene projected into range-azimuth plane. Unlike traditional SAR, the imaging space of LASAR directly corresponds to the 3-D illuminated scene. There are non-penetrating and shadow areas in the observed scene of LASAR and no scatterers in atmosphere. Consequently, scattering targets cover only a small part of the total image cells. For example, let us consider the illuminated scene in Figure 1, we can see that this scene is non-sparse for traditional SAR, but it is very sparse for LASAR because the slice of scene with the same range contains only a few scatterers, and these scatterers are extremely sparse compared to the total cells on the slice plane. Thus, spatial sparsity is a common feature in LASAR target space, which is not exploited by traditional MF-based methods at all. Due to this prior sparse feature of scatterers in 3-D space, CS is well suited for LASAR imaging.

In practice, the raw echo signals acquired by the LAA often contain strong noises. In such situations, the strong noises will affect the sparsity of echo signal and cause the precision of CS reconstruction degrade dramatically and bring about lots of artificial targets in image. In the presented method, range focussing of LASAR raw data is firstly achieved by pulse compression technique which can greatly suppress noise interference. After range compression, an appropriate basis for LASAR signal needs to be constructed. According to (1) and (5), the signal of the ith LAA element after range compression and range

migration correction can be expressed as

$$S_c(r, n, i) = \iint \left\{ \int \alpha(\mathbf{P}_w) \exp\left[j\pi f_{dr}(t - \tau)^2\right] \otimes \exp\left(-j\pi f_{dr}t^2\right) dr \right\}$$
$$\cdot \exp(-j2\pi f_c\tau)dx_s dy_s$$
$$= \iint A(r_s) \cdot \mathrm{sinc}\left[(r - r_s)/\rho_r\right]$$
$$\cdot \exp\left[-j\frac{4\pi}{\lambda} R(r, n, i; x_s, y_s)\right] dx_s dy_s$$
$$= \iint \gamma(r, n, i; x_s, y_s) \cdot \exp\left[-j\frac{4\pi}{\lambda} R(r, n, i; x_s, y_s)\right] dx_s dy_s,$$
$$1 \le n \le N_a, \ 1 \le i \le N_c \tag{8}$$

where $\gamma(r, n, i; x_s, y_s) = A(r_s) \cdot \mathrm{sinc}[(r - r_s)/\rho_r]$ is amplitude of range compression signal, and $R(r, n, i; x_s, y_s)$ denotes the distance between the scatterer on the azimuth-CT plane of range cell r and the ith LAA element position at slow time n. $\otimes$ denotes convolution symbol. For the sake of simplicity, $\gamma(r, n, i; x_s, y_s)$ and $R(r, n, i; x_s, y_s)$ are replaced by $\gamma(x_s, y_s)$ and R respectively. The distance can be expressed in Taylor series as follow

$$R = \sqrt{(x_p - x_s)^2 + (y_p - y_s)^2 + r^2} \approx R_0 + \frac{x_p^2 + y_p^2 - 2x_p x_s - 2y_p y_s}{2R_0} \tag{9}$$

where $R_0 = \sqrt{x_s^2 + y_s^2 + r^2}$ is the distance between range cell r and the reference LAA element. Furthermore, discarding the constant factor and compensating the quadratic terms, (8) can be expressed as

$$S_c(r, n, i) = \iint \gamma(x_s, y_s) \cdot \exp\left[j\frac{4\pi}{\lambda R_0}(x_s x_p + y_s y_p)\right] dx_s dy_s \tag{10}$$

Assume that the targets are point-like reflectors. The continuous space model of (10) can be approximated by discrete scatterers on the azimuth-CT plane. Let the number of image grid points in azimuth and CT directions the same as the number of pulse repeat period N_a and LAA elements N_c, respectively. Then, the total number of observed points is $N = N_a \cdot N_c$. LASAR signal in (10) can be expressed as

$$S_c(r, n, i) = \sum_{n=1}^{N_c} \sum_{i=1}^{N_a} \gamma(x_n, y_i) \cdot \exp\left[j\frac{4\pi}{\lambda R_0}(x_p x_n + y_p y_i)\right] \tag{11}$$

Converting (11) to vector form as follow.

$$S_c(r, n, i) = \psi(r, n, i)^T \gamma(r), \quad 1 \le n \le N_c, \ 1 \le i \le N_a \tag{12}$$

where $\psi(r, n, i)$ is interpreted as an N-elements measurement vector with $\psi_j = \exp[j4\pi(x_p x_j + y_p y_j)/\lambda R_0]$, $1 \leq j \leq N$ and $1 \leq p \leq N$. $\gamma(r)$ denotes an N-elements discrete reflectivity coefficient vector in the range cell r.

The received signal of azimuth-CT plane after range compression is rearranged to an N-element vector as

$$\mathbf{S}(r) = [S_c(r, 1, 1), S_c(r, 1, 2), \ldots, S_c(r, 1, N_c), \ldots, S_c(r, N_a, N_c)]^T \quad (13)$$

Then the relationship between the scattering coefficient vector $\gamma(r)$ and measured data $\mathbf{S}(r)$ can be compactly written as linear representation model.

$$\mathbf{S}(r) = \Psi(r) \cdot \gamma(r) \quad (14)$$

where $\Psi(r) \in \mathbb{C}^{N \times N}$ denotes the sparse basis function of LASAR signal after range compression. Assume the distance function $R_{pj} = x_p x_j + y_p y_j$. The basis function $\Psi(r)$ can be expressed in a form of Fourier basis matrix as follow.

$$\Psi(r) = [\psi(r, 1, 1), \psi(r, 1, 2), \ldots, \psi(r, 1, N_c), \ldots, \psi(r, N_a, N_c)]^T$$
$$= \begin{bmatrix} \exp\left(j\frac{4\pi}{\lambda R_0} R_{11}\right) & \exp\left(j\frac{4\pi}{\lambda R_0} R_{12}\right) & \ldots & \exp\left(j\frac{4\pi}{\lambda R_0} R_{1N}\right) \\ \exp\left(j\frac{4\pi}{\lambda R_0} R_{21}\right) & \exp\left(j\frac{4\pi}{\lambda R_0} R_{22}\right) & \ldots & \exp\left(j\frac{4\pi}{\lambda R_0} R_{2N}\right) \\ \vdots & \vdots & \ddots & \vdots \\ \exp\left(j\frac{4\pi}{\lambda R_0} R_{N1}\right) & \exp\left(j\frac{4\pi}{\lambda R_0} R_{N2}\right) & \ldots & \exp\left(j\frac{4\pi}{\lambda R_0} R_{NN}\right) \end{bmatrix} \quad (15)$$

According to CS theory, the sparse signal $\gamma(r) \in \mathbb{R}^N$ can be well reconstructed using only a small number of samples $M(M \leq N)$. The small number of measurements $\mathbf{S}_p$ can be obtained by projecting the signal vector $\mathbf{S}(r)$ into a sensing function Φ. To successfully reconstruct, the sensing matrix Φ must be mutually incoherent with the basis matrix Ψ, and the greater the incoherence is, the smaller number of measurements are needed. The mutual coherence can be defined as

$$\mu(\Phi, \Psi) = \max_{i,j} \frac{|\langle \phi_i, \varphi_j \rangle|}{\|\phi_i\|_2 \|\varphi_j\|_2} \quad (16)$$

where ϕ_i are rows from the measurement matrix Φ, and φ_j are columns from the basis matrix Ψ. This coherence is bounded by $1/\sqrt{N} \leq \mu(\Phi, \Psi) \leq 1$. When the value of $\mu(\Phi, \Psi)$ is $1/\sqrt{N}$, matrix Φ and Ψ are completely incoherent. In [19] and [22], it shows that random matrix performs Φ well. In this paper, we randomly select M columns for basis matrix Ψ as the measurement functions Φ. The

randomly selected matrix can be expressed as

$$\Phi = \begin{bmatrix} 1 & 0 & 0 & \dots & 0 & 0 \\ 0 & 1 & 0 & \dots & 0 & 0 \\ \vdots & \vdots & \vdots & \ddots & \vdots & \vdots \\ 0 & 0 & 0 & \dots & 0 & 1 \end{bmatrix}_{M \times N} \tag{17}$$

In this case, as all rows from matrix Φ are unit vectors, the mutually coherent $\mu(\Phi, \Psi)$ obtains the minimum value $1/\sqrt{N}$. It means that the sensing matrix Φ and the basis Ψ are completely incoherent.

Then, if we consider noise in LASAR signal, the randomly selected signal can be written as

$$\mathbf{S}_p = \Phi\Psi\gamma + \mathbf{n} = \Theta\gamma + \mathbf{n} \tag{18}$$

where $\Theta = \Phi\Psi \in \mathbb{C}^{M \times N}$ denotes the measurement matrix of LASAR signal after range compression, and $\mathbf{n}$ accounts for the additive white Gaussian noise. Θ is a random partial Fourier matrix that measures only M elements of $\gamma(r)$ located at the positions of M randomly selected columns. Hence, the measurement matrix Θ follows the RIP required in CS reconstruction. Given the observed vector $\mathbf{S}_p$ and the measurement matrix Θ, the reflectivity signal γ can be recovered from the solution of a convex optimization problem based on l_1 norm.

$$\min \|\gamma\|_1 \ \text{s.t} \ \|\mathbf{S}_p - \Theta\gamma\|_2 < \varepsilon \tag{19}$$

The detailed estimation of ε is discussed in [41]. Then in our case, if the number of randomly selected samples M meets the requirement $M \geq O(K \log(N/K))$, the resolution to (19) is exact with overwhelming probability.

4. RESULTS OF SIMULATION AND EXPERIMENTAL

In this section, some numerical simulated and real experimental data are used to evaluate the imaging performance of CS method in the case of different samples and SNR level. To compare conventional MF-based methods with CS approach, the processing is also implemented for back-projection (BP) algorithm, because it is a time-domain MF-based algorithm which can be used to sparse samples focussing.

4.1. Simulated Results

Assume that SAR platform works at altitude $H = 1000\,\text{m}$ with carrier frequency $f_c = 10\,\text{GHz}$. The bandwidth of transmitted chirp signal is $B_r = 150\,\text{MHz}$. The real aperture in azimuth is $D = 2\,\text{m}$. The number of azimuth and range samples (both obey Nyquist rate) are $N_a = 128$
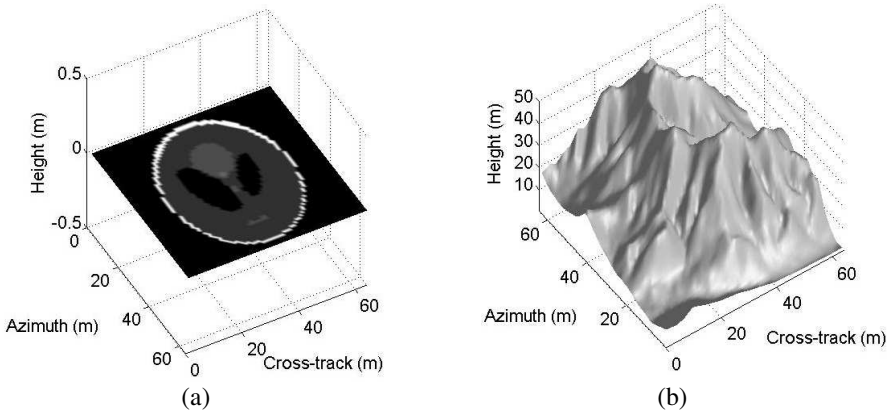
Figure 2. The original scene for simulation. (a) The Shepp-Logan phantom scene. (b) The 3-D Mount Washington terrain.

and $N_r = 128$, respectively. A full-element LAA consists of $N_c = 121$ elements. The interval of adjacent elements is 0.125 m. Then, the total length of LAA is about 15 m. According to the resolution formula of MF-based BP method in (6), the resolution of range, azimuth and CT are $\rho_r \approx 1\,\mathrm{m}$, $\rho_{at} \approx 1\,\mathrm{m}$ and $\rho_{ct} \approx 1\,\mathrm{m}$, respectively. Two discrete simulated scenes are tested, which are shown in Figures 2(a) and (b). One is a 2-D Shepp-Logan phantom, and the other is a 3-D Mount Washington terrain with the same scattering coefficients.

We first study the algorithm performance of CS method related to the number of samples. Figure 3 shows the slices of imaging results of the Shepp-Logan phantom scene using both MF-based BP and CS algorithms with different numbers of random samples ($M = 15488$, 6000, 3000, 1500 respectively). The size of the original phantom scene is 64×64 with $K = 1686$ nonzero pixels. Intuitively, the results show that traditional MF-based BP algorithm suffers from high sidelobe interferences even if total $M = 15488$ samples are used. Moreover, the sidelobes grow much larger with the number of samples decreases. Hence, the fewer measurements are used, the worse results of MF-based BP algorithm are. It is obvious that CS method successfully suppresses sidelobe and clearly reconstructs both the positions and amplitudes of actual targets, even with much less samples compared to BP algorithm. In addition, the performance of CS based method has no remarkable change when the number of randomly selected samples satisfies $M \geq O(K \log(N/K)) \approx 2160$ (in this simulation $N = 4096$, $K = 1686$), in the case of $M = 15488$, 6000, 3000. But when the sample number is smaller than 2160, for example, $M = 1500$, CS results will
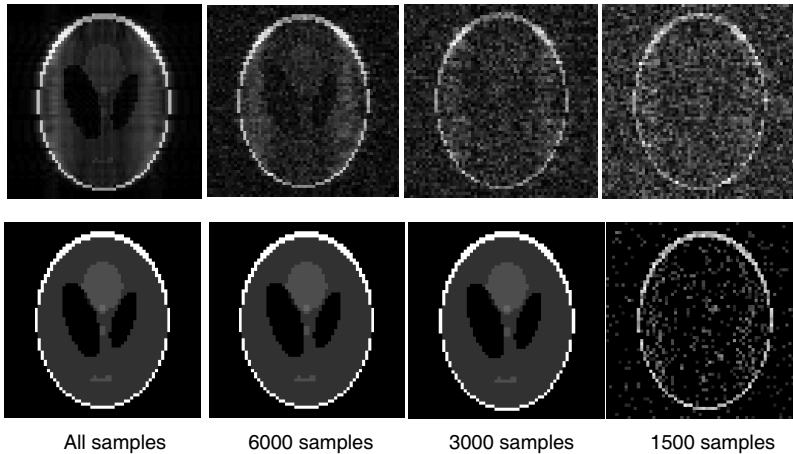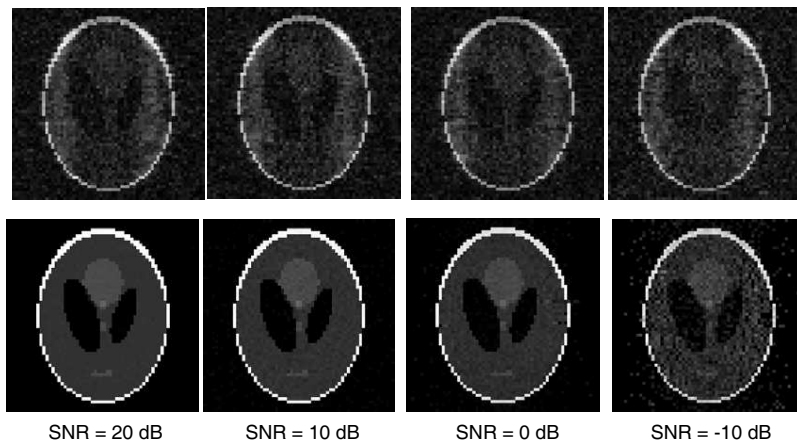
Figure 3. Imaging results of Shepp-Logan phantom with different number of samples. The top low shows the results of MF-based BP method, the bottom row shows the results of CS method. The samples number selected from left to right is all, 6000, 3000, and 1500 samples.

generate some false values in no target positions and lose some targets.

Figure 4 shows the imaging capabilities of CS method under different noise conditions compared with MF-based BP algorithm using 6000 random selected samples. An additive Gaussian white noise is added in the simulated raw echo to generate different SNR levels (SNR $= 20$ dB, 10 dB, 0 dB, -10 dB). The results demonstrate that traditional MF-based BP algorithm is robust to noise. CS method performs well for the scene reconstruction in the case of SNR $= 20$ dB, 10 dB, 0 dB. When the SNR is reduced to -10 dB, the CS method performance degrades dramatically, but still outperforms the MF-based BP algorithm. To quantitatively analyze the impact of noise on the image quality, the normal mean squared error (MSE) of MF-based BP method and CS method are plotted in Figure 5 with different SNR levels from -15 dB to 25 dB. For a given SNR, we make 100 trails Monte Carlo simulations. It is observed that the presented CS method has much smaller MSE than MF-based BP method when the SNR is larger than -10 dB, but is more sensitive to noise than BP method. According to the discussion in [25], there is a serious error for the reconstruction of CS method directly applied for SAR raw echo when SNR is lower than 10 dB. But the present CS method combined with pulse compression in range direction can achieve high resolution reconstruction for lower SNR, because range compression in CS method

can improve the amplitude and power of raw signal to $\sqrt{N_r}$ and N_r times. It means that the SNR can be increased by a factor N_r after range compression.

Figure 6 shows the imaging results of the 3-D mountain scene by MF-based BP algorithm and the CS method respectively. The echo signals are added by Gaussian white noise with SNR = 0 dB. After


Figure 4. Imaging results with different SNR level using only 6000 samples. The top low shows the results of MF-based BP method, the bottom row shows the results of CS method. The SNR level left to right are SNR = 20, 10, 0, −10 dB.
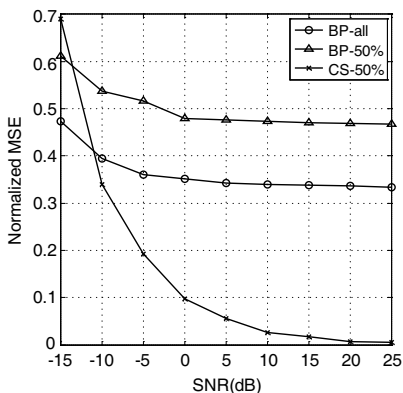
Figure 5. The normalized MSE of BP and CS method for Shepp-Logan reconstruction versus different SNR.
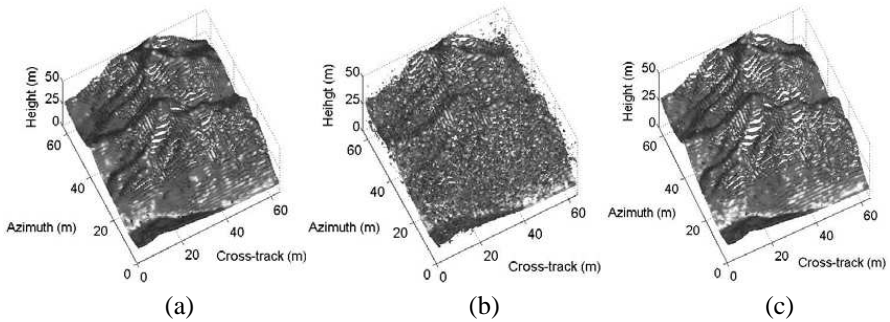
Figure 6. Reconstructed images of the 3-D mountain scene for an SNR of 0 dB. (a) MF-based BP result with all samples. (b) MF-based BP result with 1500 samples. (c) CS result with 1500 samples. The top 15 dB magnitude image voxels are displayed.
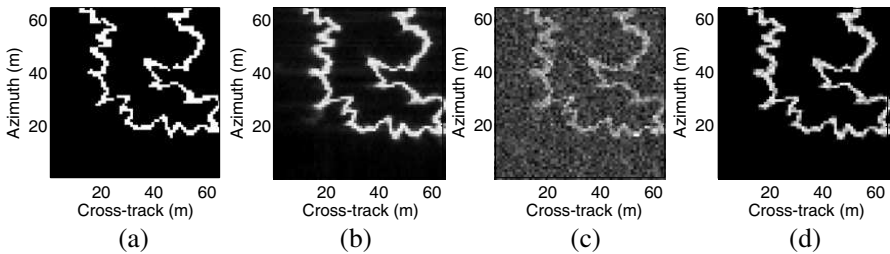

Figure 7. The slices of reconstructed results for the 3-D mountain scene. (a) Original scene. (b) MF-based BP result with all samples. (c) MF-based BP result with 1500 samples. (d) CS result with 1500 samples.

range compression, the 3-D image of MF-based BP method using all echo samples is shown in Figure 6(a). Figures 6(b) and (c) display the 3-D images received by BP and CS method with only 1500 randomly selected samples respectively. The results show that BP algorithm using 1500 echo samples suffers serious high sidelobe and generates lots of false targets in 3-D mountain area, but CS method with the same samples still obtains the correct target positions with fewer clutters. As seen obviously, the altitude slices of the original mountain scene and the reconstructed results are presented in Figure 7. The results also support the conclusion that CS method performance is better than MF-based BP method even if very small number of samples is used.

4.2. Experiments Results

In order to verify the 3-D imaging capabilities of LASAR, we have developed a ground LASAR experiment system (the detail is presented in [42]). The carrier frequency of system is $f_c = 9.618\,\mathrm{GHz}$. The bandwidth of chirp signal is $B_r = 120\,\mathrm{MHz}$ which can provide $L_c = 1.25\,\mathrm{m}$ resolution in range direction. The length of virtual LAA is designed as $1\,\mathrm{m}$ with adjacent elements interval of $0.01\,\mathrm{m}$ in this experiment. To facilitate analysis for the performance of presented CS method, a simple experiment scene is set up which only consists of some balls on the ground. Since the diameters of these balls are small enough, they can be taken as point targets. The ground LASAR system and the balls scene are shown in Figure 8(a). In Figure 8(b), the echo signal after range compression is presented, and the total samples in azimuth-CT plane is $N = 2980$.

In the first experiment, the referenced ball, which can be seen as an ideal single scatterer, is used to analyze the point spread function (PSF) of both MF-based BP method and CS method. Since range resolution is equal in both methods, for the sake of simplicity, we only give the slice images of balls in azimuth-CT plane rather than the complete 3-D images. Figure 9 shows the 2-D azimuth-CT imaging slices of the referenced ball using MF-based BP and CS method respectively. All the images are normalized to $[0, 1]$. Figure 9(a) demonstrates BP method result with all samples. Figures 9(b) and (c) display BP and CS method results with 10% samples respectively. From Figure 9, the PSF of MF-based BP method using all samples is similar to 2-D SINC function. This PSF is limited by "Rayleigh" resolution and impacted by high sidelobes. When the random samples is decreased to 10% with $M = 298$, the sidelobe in MF-based BP
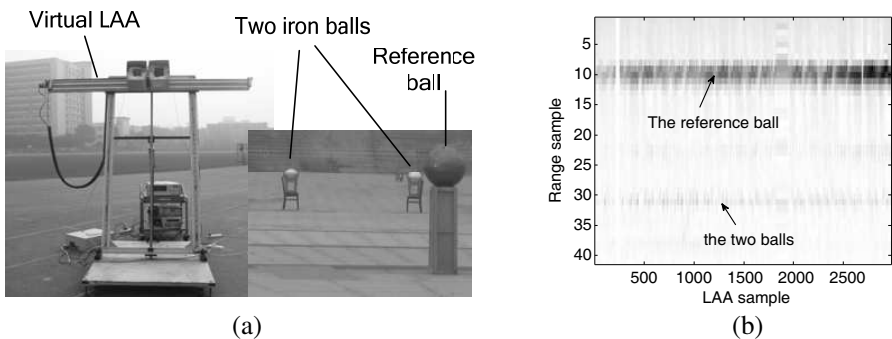
Figure 8. The ground-based LASAR experiment system and echo signal. (a) The LASAR system and the tested scene. (b) The received echo signal of the tested scene after range compression.
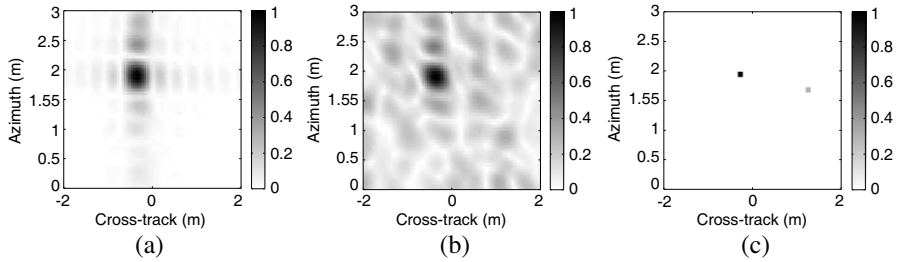
Figure 9. Images of the referenced ball on azimuth-CT plane. (a) MF-based BP result with all samples. (b) MF-based BP result with 10% samples. (c) CS result with 10% samples.
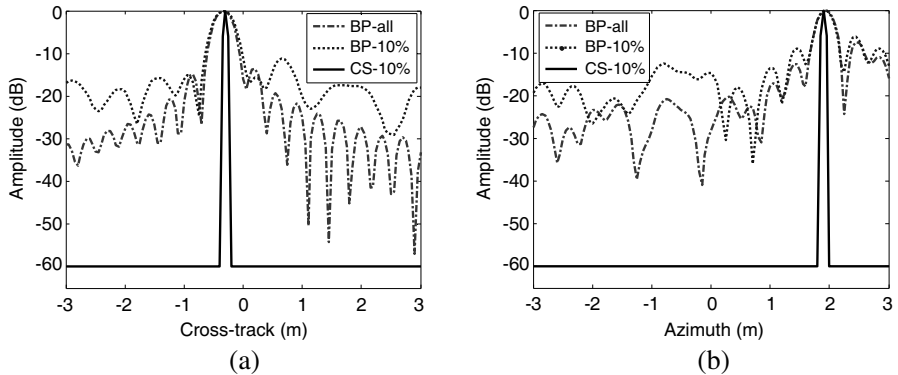

Figure 10. The PSF of the referenced ball. (a) CT direction. (b) Azimuth direction. The maximum 60 dB is displayed.

image is dramatically increased which causes target's location and amplitude fuzzy. However, CS method can faithfully reconstruct the referenced ball image with low sidelobe, and some false weak targets appear because of noise interference. The PSF of MF-based BP and CS method in azimuth and CT direction are shown in Figures 10(a) and (b), respectively. It is obvious that CS method obtains much higher resolution and lower sidelobe level than MF-based BP method even though 10% samples are used. Note that the PSF of CS in no-target positions is labeled by -60 dB. Actually the value is smaller than -60 dB in these areas.

In the second experiment, the two iron balls in the same range cell are used to verify the high resolution capability of CS method via different length of LAA. Figure 11 shows the results of BP and CS method with different lengths of LAA of 1 m, 0.5 m and 0.25 m, respectively. Here, the distance between the two scatterers is about
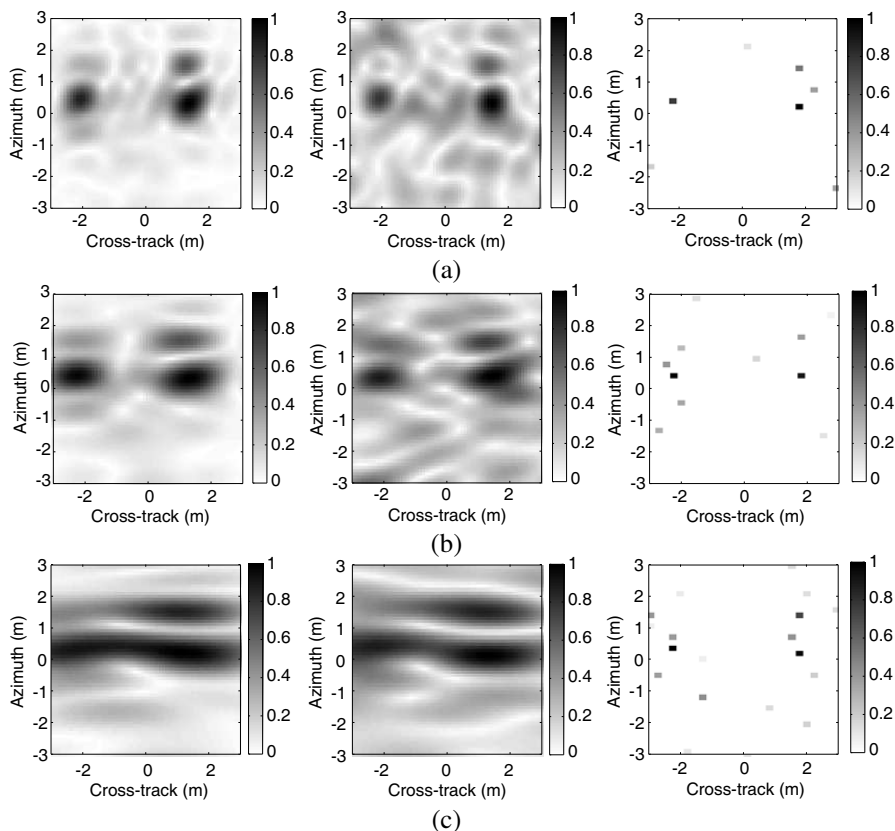
Figure 11. Images of two balls with different length of LAA (left: BP result with all samples, middle: BP result with 10% samples, right: CS result with 10% samples,). (a) The length $L = 1\,\text{m}$. (b) The length $L = 0.5\,\text{m}$. (c) The length $L = 0.25\,\text{m}$.

3.9 m in CT direction. The results demonstrate that the resolution of MF-based BP method deteriorates with the length of LAA decreases. When the length of LAA is 1 m, the ideal resolution under MF theorem is about 0.75 m. In this situation, both methods can distinguish the two scatterers clearly. However, if the length of LAA changes to 0.25 m, the ideal resolution of MF-based method is about 3.2 m. Hence BP method no longer distinguishes them clearly because their amplitudes are mixed together. But CS method still can separate them perfectly. According to the results using a small number of samples and a shorter length of LAA, the CS method still performs better than conventional MF-based BP method.

5. CONCLUSIONS

In this paper, a CS-based approach is presented for resolution enhancement and sidelobe reduction in LASAR 3-D imaging. First we accomplish range focussing by pulse compression and convert the LASAR signal model to a linear measurement model. Then a measurement matrix is constructed from randomly selected partial Fourier basis. And high resolution in azimuth-CT plane is achieved via CS l_1 norm reconstruction. Combined with pulse compression in range direction, the presented method is able to suppress strong noise interference and applied to LASAR raw data with low SNR level. Simulations and real experimental data are used to test the performance of CS method. The results demonstrate that the presented CS method can achieve much higher resolution and lower sidelobe level than the traditional MF-based BP method for LASAR imaging even with a very small number of measurements.

ACKNOWLEDGMENT

REFERENCES

1. Park, J.-I. and K.-T. Kim, "A comparative study on isar imaging algorithms for radar target identification," *Progress In Electromagnetics Research*, Vol. 108, 155–175, 2010.

2. Lazaro, A., D. Girbau, and R. Villarino, "Simulated and experimental investigation of microwave imaging using UWB," *Progress In Electromagnetics Research*, Vol. 94, 263–280, 2009.

3. Guo, D., H. Xu, and J. Li, "Extended wavenumber domain algorithm for highly squinted sliding spotlight SAR data processing," *Progress In Electromagnetics Research*, Vol. 114, 17–32, 2011.

4. Zhang, M., Y. W. Zhao, H. Chen, and W.-Q. Jiang, "SAR imaging simulation for composite model of ship on dynamic ocean scene," *Progress In Electromagnetics Research*, Vol. 113, 395–412, 2011.

5. Burgmann, R., P. A. Rosen, and E. J. Fielding, "Synthetic aperture radar interferometry to measure Earth's surface

topography and its deformation," *Annual Review of Earth and Planetary Sciences*, Vol. 28, 169–209, 2000.

6. Li, C. and D.-Y. Zhu, "A residue-pairing algorithm for insar phase unwrapping," *Progress In Electromagnetics Research*, Vol. 95, 341–354, 2009.

7. Wu, B.-I., M. C. Yeung, Y. Hara, and J. A. Kong, "Insar height inversion by using 3-D phase projection with multiple baselines," *Progress In Electromagnetics Research*, Vol. 91, 173–193, 2009.

8. Reigber, A. and A. Moreira, "First demonstration of airborne SAR tomography using multibaseline L-band data," *IEEE Transactions on Geoscience and Remote Sensing*, Vol. 38, No. 5, Part 1, 2142–2152, 2000.

9. Solimene, R., A. Brancaccio, R. Di Napoli, and R. Pierri, "3D sliced tomographic inverse scattering experimental results," *Progress In Electromagnetics Research*, Vol. 105, 1–13, 2010.

10. Teng, H. T., H.-T. Ewe, and S. L. Tan, "Multifractal dimension and its geometrical terrain properties for classification of multi-band multi-polarized SAR image," *Progress In Electromagnetics Research*, Vol. 104, 221–237, 2010.

11. Klare, J., A. Brenner, and J. Ender, "A new airborne radar for 3D imaging-image formation using the ARTINO principle," *6th European Conference on Synthetic Aperture Radar 2006*, Dresden, Germany, 2006.

12. Weiß, M., O. Peters, and J. Ender, "First flight trials with ARTINO," *7th European Conference on Synthetic Aperture Radar 2008*, Vol. 4, 187–190, 2008.

13. Du, L., Y.-P. Wang, W. Hong, et al., "A three-dimensional range migration algorithm for downward-looking 3D-SAR with single-transmitting and multiple receiving linear array antennas," *EURASIP Journal on Advances in Signal Processing*, Vol. 2010, 1–15, 2010.

14. Zhang, D.-H. and X.-L. Zhang, "Downward-looking 3-D linear array SAR imaging based on chirp scaling algorithm," *2nd Asian-Pacific Conference on Synthetic Aperture Radar (APSAR 2009)*, 1043–1046, 2009.

15. Shi, J., X.-L. Zhang, J.-Y. Yang, et al., "APC trajectory design for 'One-Active' linear-array three-dimensional imaging SAR," *IEEE Transactions on Geoscience and Remote Sensing*, Vol. 48, No. 3, 1470–1486, 2010.

16. Soumekh, M., *Synthetic Aperture Radar Signal Processing with Matlab Algorithms*, Wiley, New York, 1999.

17. Jin, Y.-Q., "Polarimetric scattering modeling and information

retrieval of SAR remote sensing — A review of FDU work," *Progress In Electromagnetics Research*, Vol. 104, 333–384, 2010.

18. Donoho, D., "Compressed sensing," *IEEE Trans. Inf. Theory*, Vol. 52, No. 4, 1289–1306, Apr. 2006.

19. Candes, E. J. and M. Wakin, "An introduction to compressive sampling," *IEEE Signal Processing Magazine*, 21–30, Mar. 2008.

20. Patel, V. M., G. R. Easley, and D. M. Healy, "Compressed synthetic aperture radar," *IEEE Journal of Selected Topics in Signal Processing*, Vol. 4, No. 2, 244254, Apr. 2010.

21. Herman, M. A. and T. Strohmer, "High-resolution radar via compressed sensing," *IEEE Trans. on Signal Processing*, Vol. 57, No. 6, 2275–2284, Jun. 2009.

22. Zhang, L., M.-D. Xing, C.-W. Qiu, et al., "Achieving higher resolution ISAR imaging with limited pulses via compressed sampling," *IEEE Transactions on Geoscience and Remote Sensing*, Vol. 4, No. 2, 567–571, 2009.

23. Liu, Y.-B., Y.-H. Quan, J. Li, et al., "SAR imaging of multiple ships based on compressed sensing," *2nd Asian-Pacific Conference on Synthetic Aperture Radar (APSAR 2009)*, 112–115, 2009.

24. Potter, L. C., E. Ertin, J. T. Parker, and M. Çetin, "Sparsity and compressed sensing in radar imaging," *Proceedings of the IEEE*, Vol. 98, No. 6, 1006–1020, 2010.

25. Wei, S.-J., X.-L. Zhang, J. Shi, and G. Xiang, "Sparse reconstruction for SAR imaging based on compressed sensing," *Progress In Electromagnetics Research*, Vol. 109, 63–81, 2010.

26. Zhu, X.-X. and R. Bamler, "Tomographic SAR inversion by L1-norm regularization — The compressive sensing approach," *IEEE Transactions on Geoscience and Remote Sensing*, Vol. 48, No. 10, 3839–3846, 2010.

27. Budillon, A., A. Evangelista, and G. Schirinzi, "Three-dimensional SAR focussing from multipass signals using compressive sampling," *IEEE Transactions on Geoscience and Remote Sensing*, Vol. 49, No. 1, 488–499, 2010.

28. Chan, Y. K. and V. C. Koo, "An introduction to Synthetic Aperture Radar (SAR)," *Progress In Electromagnetics Research B*, Vol. 2, 27–60, 2008.

29. Chua, M. Y. and V. C. Koo, "FPGA-based chirp generator for high resolution UAV SAR," *Progress In Electromagnetics Research*, Vol. 99, 71–88, 2009.

30. Lim, S.-H., J.-H. Han, S.-Y. Kim, and N.-H. Myung, "Azimuth beam pattern synthesis for airborne SAR system optimization,"

Progress In Electromagnetics Research, Vol. 106, 295–309, 2010.

31. Sun, J., S. Mao, G. Wang, and W. Hong, "Polar format algorithm for spotlight bistatic SAR with arbitrary geometry configuration," *Progress In Electromagnetics Research*, Vol. 103, 323–338, 2010.

32. Chan, Y. K. and S. Y. Lim, "Synthetic Aperture Radar (SAR) signal generation," *Progress In Electromagnetics Research B*, Vol. 1, 269–290, 2008.

33. Nie, X., D.-Y. Zhu, and Z.-D. Zhu, "Application of synthetic bandwidth approach in SAR polar format algorithm using the deramp technique," *Progress In Electromagnetics Research*, Vol. 80, 447–460, 2008.

34. Sabry, R. and P. W. Vachon, "Advanced polarimetric synthetic aperture radar (SAR) and electro-optical (EO) data fusion through unified coherent formulation of the scattered EM field," *Progress In Electromagnetics Research*, Vol. 84, 189–203, 2008.

35. Crowgey, B. R., E. J. Rothwell, L. C. Kempel, and E. L. Mokole, "Comparison of UWB short-pulse and stepped-frequency radar systems for imaging through barriers," *Progress In Electromagnetics Research*, Vol. 110, 403–419, 2010.

36. Sun, J., S. Mao, G. Wang, and W. Hong, "Polar format algorithm for spotlight bistatic SAR with arbitrary geometry configuration," *Progress In Electromagnetics Research*, Vol. 103, 323–338, 2010.

37. Chen, S., D. Donoho, and M. A. Saunders, "Atomic decomposition by basis pursuit," *SIAM J. Sci. Comput.*, Vol. 20, No. 1, 33–61, 1999.

38. Tropp, J. A., "Greed is good: Algrorithm results for sparse approximation," *IEEE Trans. Inf. Theory*, Vol. 50, No. 10, 2231–2242, Oct. 2004.

39. Needell, D. and R. Vershynin, "Uniform uncertainty principle and signal recovery via regularized orthogonal matching pursuit," *Found Comput. Math.*, Vol. 9, No. 3, 317–334, Jun. 2009.

40. Candes, E. J., J. K. Romberg, and T. Tao, "Robust uncertainty principles: Exact signal reconstruction from highly incomplete frequency information," *IEEE Trans. Inf. Theory*, Vol. 52, No. 2, 489–509, Feb. 2006.

41. Candes, E. J., J. K. Romberg, and T. Tao, "Stable signal recovery from incomplete and inaccurate measurements," *Communications on Pure and Applied Mathematics*, Vol. 59, No. 8, 1207–1223, 2006.

42. Shi, J., X.-L. Zhang, J.-Y. Yang, et al., "Experiment results on 'one-active' LASAR," *IEEE Radar Conference*, 1–4, 2009.